



HAL
open science

Induction in a von Kármán flow driven by ferromagnetic impellers

Gautier Verhille, Nicolas Plihon, Mickaël Bourgoïn, Philippe Odier,
Jean-François Pinton

► **To cite this version:**

Gautier Verhille, Nicolas Plihon, Mickaël Bourgoïn, Philippe Odier, Jean-François Pinton. Induction in a von Kármán flow driven by ferromagnetic impellers. *New Journal of Physics*, 2010, 12, pp.033006. 10.1088/1367-2630/12/3/033006 . hal-00440853v2

HAL Id: hal-00440853

<https://hal.science/hal-00440853v2>

Submitted on 13 Apr 2015

HAL is a multi-disciplinary open access archive for the deposit and dissemination of scientific research documents, whether they are published or not. The documents may come from teaching and research institutions in France or abroad, or from public or private research centers.

L'archive ouverte pluridisciplinaire **HAL**, est destinée au dépôt et à la diffusion de documents scientifiques de niveau recherche, publiés ou non, émanant des établissements d'enseignement et de recherche français ou étrangers, des laboratoires publics ou privés.

Induction in a von Kármán flow driven by ferromagnetic impellers

Gautier Verhille¹, Nicolas Plihon¹, Mickal Bourgoïn²,
Philippe Odier¹ and Jean-François Pinton^{1,3}

¹Laboratoire de Physique, CNRS & École Normale Supérieure de Lyon,
UMR5672, Université de Lyon, 46 allée d'Italie, F69007 Lyon, France

²Laboratoire des Écoulements Géophysiques et Industriels, CNRS/UJF/INPG
UMR5519, BP53, F38041 Grenoble, France

E-mail: pinton@ens-lyon.fr

New Journal of Physics **12** (2010) 033006 (13pp)

Received 13 December 2009

Published 9 March 2010

Online at <http://www.njp.org/>

doi:10.1088/1367-2630/12/3/033006

Abstract. We study magnetohydrodynamics in a von Kármán flow driven by the rotation of impellers made of material with varying electrical conductivity and magnetic permeability. Gallium is the working fluid and magnetic Reynolds numbers of order unity are achieved. We find that specific induction effects arise when the impellers' electric and magnetic characteristics differ from that of the fluid. Implications with regard to the VKS dynamo are discussed.

Contents

1. Introduction	2
2. Experimental setup	2
3. Induction linked to differential rotation	4
3.1. Induction from an axial applied field	4
3.2. Induction from a transverse applied field	5
4. Interpretation	8
4.1. An induction mechanism associated with a jump of magnetic diffusivity at the impellers	8
4.2. Illustration: induction effects linked to helicity	10
5. Discussion and conclusions	12
Acknowledgments	12
References	12

³ Author to whom any correspondence should be addressed.

1. Introduction

The choice of electromagnetic boundary conditions in dynamo studies, and its implications on underlying magnetohydrodynamic processes, has long been an open issue. In experiments, a finite flow of an electrically conducting fluid is generally considered, and the outer medium is ultimately electrically insulating (with electromagnetic properties of vacuum). Studies have considered layers with various properties regarding electrical conductivity σ_w and/or magnetic permeability μ_w . Motivations for this have varied considerably. In many numerical simulations, it has been computationally convenient to assume an infinite value of μ_w , yielding an attachment of magnetic field lines normal to the wall [1]. In some simulations of the geodynamo, a thin-wall approach [2] has been implemented in order to account for the rapid changes in electrical conductivity at the core–mantle boundary [3, 4]. Experiments have tended to extensively study changes with boundary conditions. The motivation is that the critical magnetic Reynolds number value for the onset of dynamo action must be lowered as much as possible in order to lie within reach of a given experimental facility. For instance, in the pioneering experiments in Riga and Karlsruhe, a volume of stagnant liquid sodium around the flow was found to be very favorable [5, 6]. In the same spirit, dynamo action in the von Kármán sodium (VKS) experiment [7] has only been observed in situations where the fluid is driven by the motion of soft iron impellers. When replaced by non-magnetic stainless steel impellers, no dynamo was generated at the highest stirring achievable with the mechanical drives. In addition, the dominant VKS dynamo mode is essentially an axisymmetric dipole, in contradiction with predictions based on the mean flow structure [8, 9]. It is the motivation of this work to better understand the influence of the boundary conditions imposed by the ferromagnetic impellers, in particular whether they significantly change the induction processes or simply lower the threshold of a dynamo that would be reached at higher rotation rates of non-magnetic impellers, if that was possible. To this end, we have performed extensive induction measurements in a gallium von Kármán flow driven by impellers made of stainless steel, copper or soft iron.

The experimental device is first described. Induction measurements are then presented and detailed in section 3. A physical interpretation of these measurements is developed in section 4. In section 5, we present a discussion of the impact of these mechanisms on the VKS experiments.

2. Experimental setup

A von Kármán flow is produced by the coaxial rotation of two impellers inside a stainless steel cylindrical vessel filled with liquid gallium—cf figure 1(a). The cylinder radius R is 97 mm and its length is 323 mm. The impellers have a radius equal to 82.5 mm and are fitted to a set of eight straight blades with height 10 mm. The impellers are separated by a distance $H = 203$ mm. They are driven by two ac motors that provide a constant rotation rate in the interval $(F_1, F_2) \in [0.5, 25]$ Hz.

In most cases, the flow is driven by symmetric counter-rotation of the impellers at $F_1 = F_2 = F$. It is structured in two rotating cells in front of each impeller, separated by a large azimuthal shear layer in the mid-plane of the cylinder. Driving can also be achieved using the rotation of one single disk, the other being at rest; the flow then consists of a single rotating cell. In both cases, the fluid is also ejected radially outward by the rotating disk(s); this drives an axial flow toward them along the cylinder axis and a recirculation in the opposite direction along the cylinder lateral boundary.

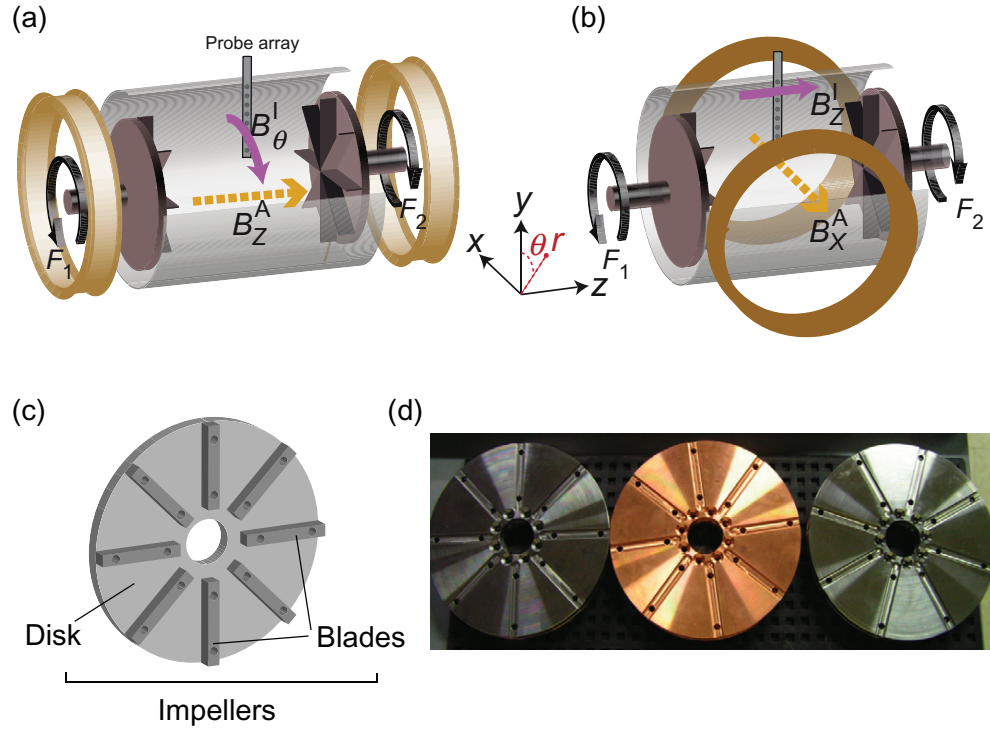


Figure 1. A von Kármán flow of liquid gallium is generated in a cylindrical vessel between two counter-rotating impellers driven by two ac motors. (a) When an axial field B_z^A is applied, the counter-rotating flow induces an azimuthal magnetic field B_θ^I in the mid-plane of the flow. A radial profile of this field is recorded by a linear probe array of Hall sensors. (b) When a transverse field B_x^A is applied, an axial component B_z^I is induced in the center, in a plane perpendicular to the applied field. (c) Schematic and (d) pictures of the impellers used in this study: disks and blades can be assembled independently from elements made of stainless steel, copper or soft iron.

The system is cooled by water circulation located behind the driving impellers; the experiments are run at a temperature between 40 and 48 °C. Liquid gallium has density $\rho = 6.09 \times 10^3 \text{ kg m}^{-3}$ and electrical conductivity $\sigma = 3.68 \times 10^6 \text{ } \Omega^{-1} \text{ m}^{-1}$, and hence a magnetic diffusivity $\lambda = 1/\mu_0\sigma = 0.22 \text{ m}^2 \text{ s}^{-1}$. Its kinematic viscosity is $\nu = 3.1 \times 10^{-7} \text{ m}^2 \text{ s}^{-1}$. The integral kinematic and magnetic Reynolds numbers are defined as $Re = 2\pi R^2 F/\nu$ and $R_m = 2\pi R^2 F/\lambda$. By varying F , values of R_m up to 5 are achieved, with corresponding Re values in excess of 10^6 .

Two pairs of induction coils (in a Helmholtz configuration) are aligned parallel to the rotation axis or perpendicular to it. They create an applied magnetic field \mathbf{B}^A of a few tens of gauss inside the vessel, essentially uniform in the direction of the axis of the coils. The interaction parameter $N = \sigma (B^A)^2 / 2\pi\rho F \sim 10^{-5}$ is small, so that the action of Lorentz forces on the flow can be neglected. Magnetic induction measurements are performed using a Hall sensor probe array (eight probes) inserted into the flow in the mid-plane. Data are recorded using a National Instrument PXI-4472 digitizer at a rate of 1000 Hz with 23-bit resolution.

Table 1. Relative magnetic permeability (μ_r), electrical conductivity (σ) and magnetic diffusivity (λ) of the materials, using stainless steel (ss) as a reference. Values taken from [12], except for iron permeability, which was experimentally measured—see text.

	Stainless steel	Copper	Soft iron	Gallium
μ_r	1	1	65	1
σ ($\times 10^6 \Omega^{-1} \text{ m}^{-1}$)	$\sigma_{\text{ss}} = 1.4$	$42 \sigma_{\text{ss}}$	$7.3 \sigma_{\text{ss}}$	$2.6 \sigma_{\text{ss}}$
$\lambda^{-1} = \mu\sigma$ ($\text{m}^{-2} \text{ s}$)	$\lambda_{\text{ss}}^{-1} = 1.8$	$42 \lambda_{\text{ss}}^{-1}$	$475 \lambda_{\text{ss}}^{-1}$	$2.6 \lambda_{\text{ss}}^{-1}$

The impellers driving the flow are made of a flat disk upon which straight blades are fixed. In the study reported here, both the disk and the blades can be chosen independently from stainless steel, copper or soft iron. These materials are characterized by their electrical conductivity and magnetic permeability. For stainless steel and copper, the permeability is equal to that of vacuum, $\mu_0 = 4\pi \times 10^{-7} \text{ H m}^{-1}$. The permeability of soft iron is known to change significantly during the manufacturing process. We have measured its value after machining from the B – H response curves for small-amplitude magnetic fields, using the procedure described in [10]: a flux-meter is set on a soft iron blade and one on a copper blade, both placed in a time-varying H -field, so as to build the hysteresis cycle of the soft iron $B = f(H)$. The permeability of soft iron is then computed from the slope $\partial B / \partial H$ when $H \rightarrow 0$. The electrical and magnetic properties of the material used in this study are summarized in table 1. Note that we checked experimentally and numerically—using FEMM 4.2 software [11]—that, with liquid gallium at rest and in the case of soft-iron impellers, the effect of the high permeability of the materials produces only a weak distortion of the magnetic field applied by the coils at the probe location as compared to stainless steel impellers.

3. Induction linked to differential rotation

The swirling flow generated by the exact counter-rotation of the impellers ($F_1 = F_2 = F$) possesses a large shear layer in the mid-plane of the cylinder [13]. Induction effects are generated by this azimuthal shear. We study the variation of their amplitude and radial profile, as the impellers are counter-rotated with increasing rotation rate F and the impeller materials varied.

3.1. Induction from an axial applied field

We first investigate the case where the applied field is coaxial to the cylinder: $\mathbf{B}^A = B_z^A \hat{z}$. This configuration is sketched in figure 1(a). When stainless steel impellers are used, the induced magnetic field along the azimuthal direction, denoted B_θ^I , is due to the ω -effect, and is proportional to the fluid differential rotation $\partial_z v_\theta$ [14]–[16].

We now consider possible changes of this induction effect caused by driving the flow with impellers of varying materials. The radial profiles (in the median plane xOy) of the time-averaged induced azimuthal field, $\langle B_\theta^I \rangle$, are shown for $F = 12 \text{ Hz}$ in figure 2. Impellers made of stainless steel, copper or iron have been used (in this case, disks and blades are made of the same material). In figure 2(a), magnetic data are normalized to their maximum value in order to compare the induction *profiles*. We observe that they do not change noticeably when the

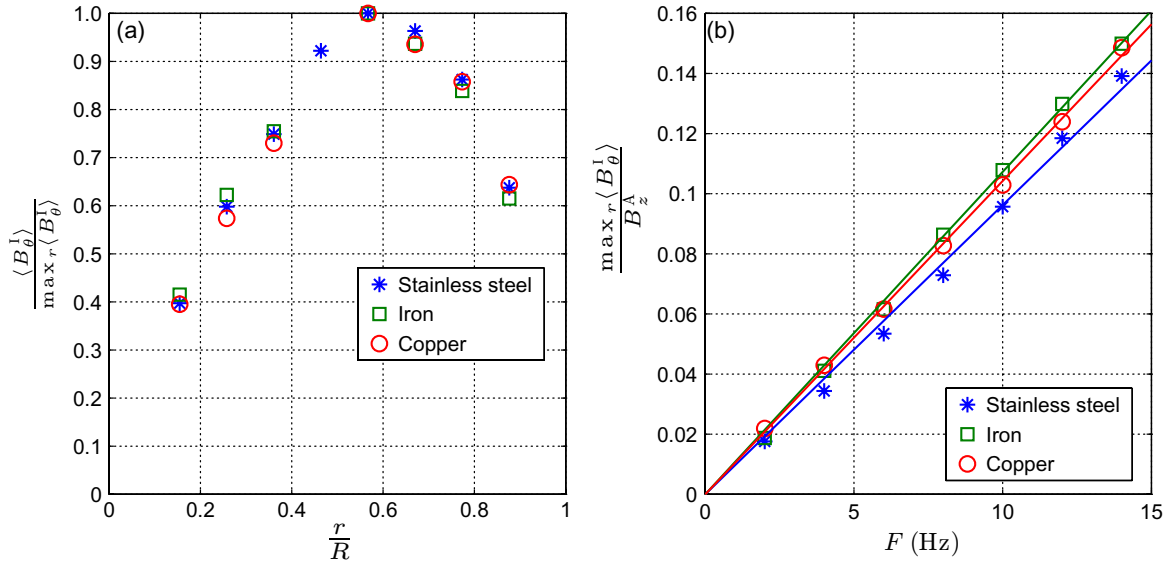


Figure 2. Time-averaged ω -effect with an axially imposed field B_z^A . (a) Radial profiles of the induced field $\langle B_\theta^I \rangle$ at $F = 12$ Hz for impellers made of stainless steel (\star), iron (\square) and copper (\circ). Profiles are normalized to the maximum of $\langle B_\theta^I \rangle$ along the radius ($\max_r \langle B_\theta^I \rangle$). (b) Evolution of the maximum of $\langle B_\theta^I \rangle$ along the radius normalized to the imposed field B_z^A as a function of impeller rotation frequency (symbols as in (a)).

material of the impellers is varied. The profiles are also independent of the impellers' rotation rate. Figure 2(b) shows the evolution of the maximum amplitude of these radial profiles with the rotation rate F . One observes that the impeller material has a very weak influence here. Induction can be understood as the usual ω -effect due to fluid motions (linear in flow forcing and proportional to the time-averaged fluid differential rotation $\langle \partial_z v_\theta \rangle$) with no noticeable influence of impeller material. Note that all field amplitudes have been normalized to the applied field measured at the probe location, thus taking into account the weak local distortion of the applied field lines in the case of the soft-iron impellers (the variation is weak—less than 10%).

Given the very high Reynolds number value of the flow, the induced magnetic field has a turbulent signature, with fluctuations as high as the time-averaged amplitude (see for instance [14]). The evolution of the rms amplitude of the fluctuations as a function of the impellers' rotation rate is displayed in figure 3(a). It is linear in F and the dispersion between data obtained for impellers made of the three materials is less than 5%. The PDF and PSD at $F = 12$ Hz are shown in figures 3(b) and (c), respectively. These measurements show that no significant change in the fluctuations of the ω -effect can be observed as the impeller material is varied at the location of the measurements, i.e. here in the mid-plane, cf section 4.

3.2. Induction from a transverse applied field

In this section, we address the issue of induction from a transverse applied field: $\mathbf{B}^A = -B_x^A \hat{x}$. This configuration is sketched in figure 1(b). The induced magnetic field is probed along the axial direction, B_z^I .

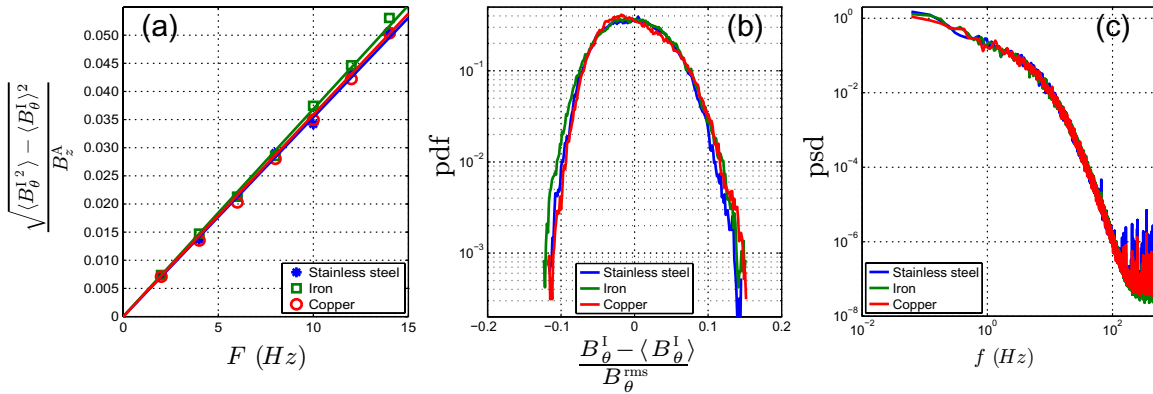


Figure 3. Fluctuations of the ω -effect with an axially imposed field B_z^A . (a) Evolution of the standard deviation of B_θ^I as a function of the impeller rotation rate F for impellers made of stainless steel (\star), iron (\square) and copper (\circ). (b) Corresponding probability density function (PDF) and (c) power spectrum density (PSD) for $F = 12$ Hz and impellers made of stainless steel (blue), iron (green) and copper (red).

For the case of a flow driven by stainless steel impellers and enclosed in a stainless steel vessel, the induction processes at work here have been described in detail in [15, 16] (in particular, see figure 13 in [16]) and will only be recalled here. Near the impellers, the flow rotational motion advects the imposed magnetic field B_x^A , so as to induce a perpendicular component B_y^I . With the rotation opposite on either side of the flow mid-plane, two such contributions (with opposite directions) are generated on each side. These induced fields are associated with a current distribution consisting of two current sheets in the direction of the applied field, one in each flow cell, plus one with opposite direction in the shear layer. This generates an axial field B_z^I , maximum in a plane transverse to the applied field. This effect, directly linked to the rotation of the fluid, is linear in F . As in [16] we will refer to this induction process as a BC effect in what follows, since it originates in the boundary conditions from the steep variation in electrical conductivity at the vessel wall. A simplified way of understanding this effect is to consider the B_z^I component in the mid-plane as resulting from the reconnection path of the B_y^I contributions on either side.

As before, we study modifications of this induction process resulting from changing the impeller material. For the three materials used, the radial profiles of the normalized time-averaged induced axial field $\langle B_z^I \rangle$ are shown in figure 4(a). These normalized profiles are again independent of impeller rotation rate and impeller material. Since the *profiles* are unchanged, one may suppose that a similar BC mechanism can be invoked in all cases. In addition, in the low R_m regimes accessible in the device, the BC effect remains linear in R_m whatever the impeller material. However, as seen in figure 4(b), the *amplitude* of the time-averaged induced field now strongly depends on the impeller material: a 20% increase for copper and a 220% increase for soft iron are measured, as compared to stainless steel impellers.

As shown in figure 5, changes in the rms intensity of the fluctuations of induction are much more modest. Variations are very small between stainless steel and copper impellers. Soft iron generates a 10% increase of the fluctuation level compared to the other, non-magnetic, materials.

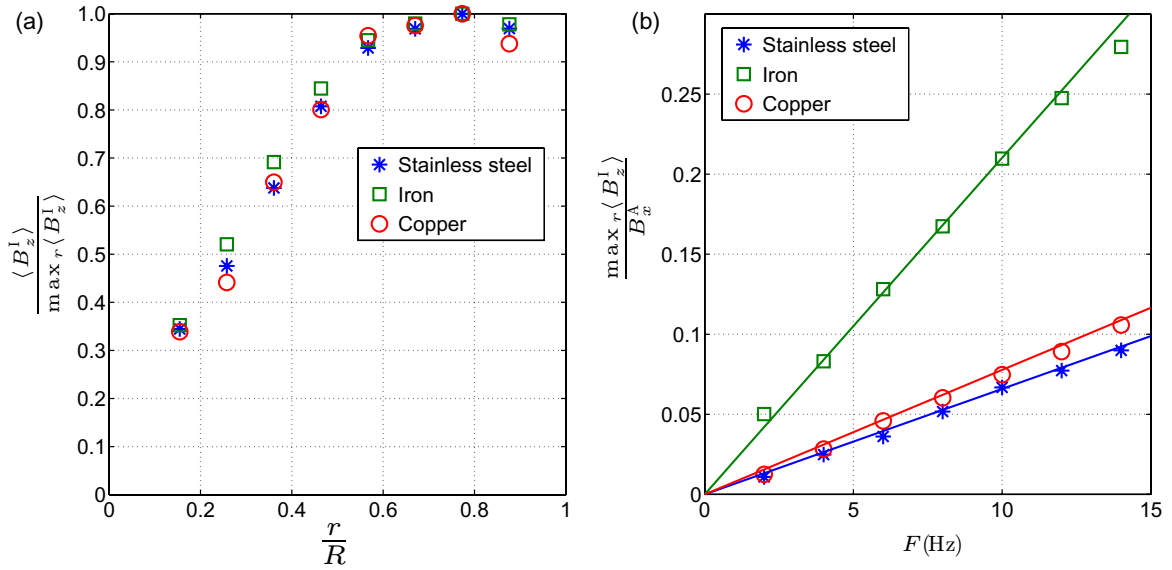


Figure 4. Time-averaged BC effect with a transverse imposed field B_x^A . (a) Radial profiles of the induced field $\langle B_z^I \rangle$ at $F = 12$ Hz for impellers made of stainless steel (\star), iron (\square) and copper (\circ). Profiles are normalized to the maximum of $\langle B_z^I \rangle$ along the radius ($\max_r \langle B_z^I \rangle$). (b) Evolution of the maximum of $\langle B_z^I \rangle$ along the radius, normalized to the imposed field B_x^A , as a function of impeller rotation frequency (symbols as in (a)).

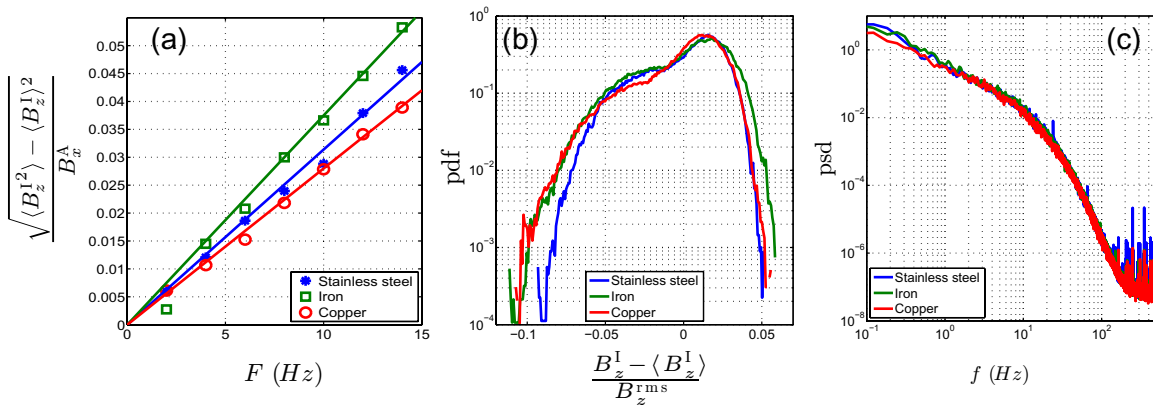


Figure 5. Fluctuations of the BC-effect with a transverse imposed field B_x^A . (a) Evolution of the standard deviation of B_z^I as a function of the impeller rotation rate F for impellers made of stainless steel (\star), iron (\square) and copper (\circ). (b) Corresponding PDF and (c) PSD at $F = 12$ Hz for impellers made of stainless steel (blue), iron (green) and copper (red).

This may be a second-order effect: as the mean axial component $\langle B_z^I \rangle$ is increased, its stretching by fluctuations of the axial velocity gradient may add to the rms intensity. Time spectra are, however, identical in the frequency range usually attributed to turbulent motions—figure 5(c).

The bimodal distribution in figure 5(b) is known to originate from the non-stationarity of the shear layer in the mid-plane [17, 18]. Its shape remains fairly independent of the impeller's nature. Fluctuations of the induced field are thus not essentially modified by a change of impeller material. This may be expected since the magnetic field fluctuations trace back to the flow turbulence, which is not expected to be affected by impeller material.

We argue in section 4 that the increase in the mean induced component $\langle B_z^I \rangle$ arises in a process similar to the one described in [16] from a localized ω -effect generated when the magnetic diffusivity of the impellers differs from that of the fluid.

4. Interpretation

4.1. An induction mechanism associated with a jump of magnetic diffusivity at the impellers

When probing induction effects in the mid-plane, our observations so far can be summarized as follows:

- In the case of an axial applied field (induction from differential rotation in the fluid bulk), the induced field seems to be fairly independent of impeller material.
- In the case of a transverse applied field (induction from differential rotation, coupled with insulating boundary conditions), the time-averaged amplitude of the induced field varies strongly with impeller material.
- In both cases, the spatial profile of the induced field is independent of the impellers' nature, and the fluctuations of induction are not appreciably changed.

In order to interpret these observations, we need to understand the role of variations of magnetic diffusivity at the gallium–impeller interface on induction effects. We begin with the case of the transverse applied field, which shows the strongest dependence on the impellers nature. Herzenberg and Lowes have studied the case of a finite cylinder rotating at frequency Ω in a uniform field perpendicular to the cylinder axis. To leading order, equation (4.12) of [19] for the induced magnetic field is written

$$\mathbf{B}^I(r, \theta, \phi) = \frac{1}{32\pi^2} (2\pi \mu \sigma \Omega a^2) B^A V_{\text{cyl}} \hat{z} \times \nabla \left(\frac{\sin \theta \cos \phi}{r^2} \right), \quad (1)$$

where (r, θ, ϕ) are spherical coordinates with origin at the center of the cylinder of radius a and V_{cyl} is the volume of the cylinder. In the above derivation, the cylinder and medium are assumed to have the same magnetic diffusivity, and the medium outside the cylinder is at rest. This induced field has approximately the geometry of a dipole with its axis perpendicular both to the axis of rotation and to the applied field. Its amplitude can also be written as $B^I \propto B^A R_m^{\text{cyl}} (V_{\text{cyl}}/r^3)$, with $R_m^{\text{cyl}} = \mu \sigma (2\pi a \Omega) a$ the magnetic Reynolds number of the rotating cylinder. It corresponds to a (radial) ω -effect, due to the shearing of the magnetic field lines that are 'advected' by cylinder rotation; it is also the first step of the expulsion of the transverse field from the rotating body [20]. If we now consider a situation where the cylinder is made of a material with a different magnetic diffusivity, a similar induced field will be generated, even if the fluid around the cylinder rotates with the same velocity, i.e. if there is no differential rotation. This is because a change in magnetic permeability or a change in electrical conductivity also contributes to the induction processes. For instance, if the cylinder has a higher permeability, then the higher values of the flux of \mathbf{B} in the cylinder will generate a shear of field lines at the

fluid boundary. If the cylinder has a better electrical conductivity, then the same flux variation will be able to generate more induced currents. Altogether it is an effective change in the magnetic diffusivity $\mu\sigma$ that matters here (although changes in μ and σ cannot be completely equivalent because they are associated with different boundary conditions).

These arguments, supported by recent numerical works [21, 22], have led us to write the correction to homogeneous induction effects, in a first approximation, as

$$B^I \propto B^A (R_m^{\text{cyl}} - R_m^{\text{fluid}}) \frac{V_{\text{cyl}}}{r^3} \quad (2)$$

for the induction generated by a local jump of either magnetic diffusivity or velocity at the cylinder end.

We then return to our induction measurements, as reported in the previous section. In the case of an applied field transverse to the flow axis, the rotation of each impeller creates an induced perpendicular dipole (as above). As in the BC effect, the reconnection of these induced fields and the constraints on current paths create an axial component in the (yOz) plane. This field will add to the axial field induced by the usual BC mechanism. This explanation accounts for the very similar induction profile observed (see figure 4(a)) with different materials used for the impellers: the additional effect due to the impellers is produced by a mechanism with a geometry identical to that of the BC effect. It also explains why the impeller material has so little effect on the fluctuations of induction: the source of induction lies in the rotation of the impellers that is precisely controlled in the experiment to be constant in time, fixed to a prescribed value. Fluctuations are essentially due to changes in the induction generated by velocity gradients within the flow, which have a quite non-stationary (turbulent) dynamics [18].

We thus write the axial induced field measured in the mid-plane as being the sum of two contributions: (i) the regular BC effect, which originates from the differential rotation of the fluid, and (ii) the effect described above, caused by the change in magnetic diffusivity at the impellers: $B_z^I = B_z^I(\text{fluid}) + B_z^I(\text{at impellers})$, i.e.

$$\frac{B_z^I}{B^A} = K_f R_m + K_i R_m \left(\frac{(\mu\sigma)_i}{(\mu\sigma)_f} - 1 \right) \frac{V_i}{V_i^{\text{max}}}, \quad (3)$$

where $K_{f,i}$ are constants taking into account the precise location of the measurement, and the second term has been chosen to emphasize two features: (i) no additional effect occurs when the impellers have magnetic diffusivity that matches that of the fluid (all is then incorporated in the first term); (ii) the ratio V_i/V_i^{max} accounts for the fact that at each impeller, disk and blades can be made of different materials; V_i^{max} is the maximum volume of disk plus blades, and V_i is the actual volume of a given material in the impeller (which can be disk and/or blade) so that the effective volume fraction is less than one — $V_i < V_i^{\text{max}} = 3.15 \times 10^{-4} \text{ m}^3$.

By varying separately blade and disk materials, and performing measurements for a range of rotation rates of the impellers, one may thus probe the above relationship. Figure 6 (blue circles) shows the slopes $(d(B_z^I/B^A))/(dR_m)$ as a function of the impeller parameter $((\mu\sigma)_i/(\mu\sigma)_f - 1)V_i/V_i^{\text{max}}$. The linear behavior expected from equation (3) is indeed observed: one measures $K_f = 2.4 \times 10^{-2}$ and $K_i = 3.9 \times 10^{-4}$. The horizontal error bars are fairly large, since there is a non negligible uncertainty in computing the actual volume of the impellers that plays a role in the induction effect. This is because the blades are indeed attached with stainless steel screws that may prevent the optimal development of electrical currents in more conducting materials.

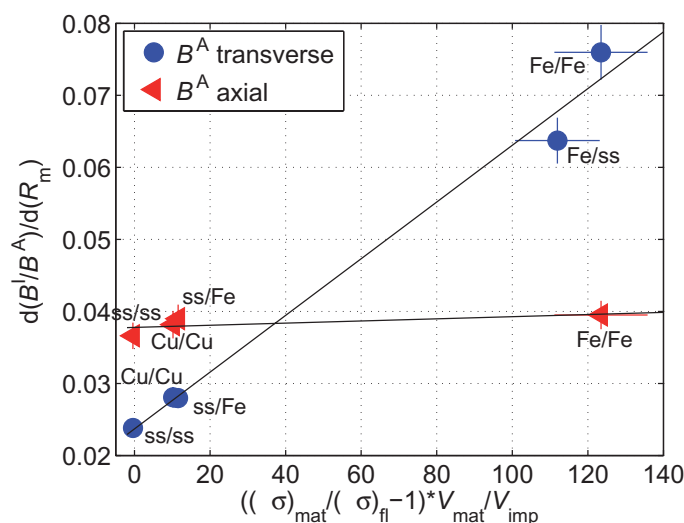


Figure 6. Slopes of curves B^I/B^A as a function of R_m , for the different configurations studied, as a function of $(\mu\sigma)_i/(\mu\sigma)_f - 1) V_i/V_i^{\max}$ when the material of the disk and that of the blades are changed. The combinations used are indicated in the figure, with the first mention corresponding to the disk and the second to the blades. ‘ss’ stands for stainless steel, ‘Fe’ for iron and ‘Cu’ for copper. The blue circles correspond to the case of a transverse applied field and the red triangles to the axial applied field.

The inhomogeneity of magnetic diffusivity at the impellers is also expected to produce an added induction in the case of an axially applied field—in this case, however, a velocity shear at the fluid–impeller interface is necessary (otherwise no variation of flux can cause induction). Using again the calculation by Herzenberg and Lowes [19] as a reference, one expects a variation of the azimuthal-induced field with disks and blades materials. Figure 6 (red triangles) shows that it is indeed the case, but the evolution is much shallower. The explanation lies in the fact that the effect is localized in the vicinity of the impellers—it decays as the inverse third power of the distance to the disk [19] (equation (3.21)) and, in this case, there is no global effect of the boundary condition that constrains the currents and helps ensure that a sizable magnetic field can be detected in the mid-plane of the flow (where the measurement probes are located).

We thus find that our interpretation, which attributes the induction to conventional effects from the shearing motion of the fluid plus an additional contribution due to the inhomogeneity of the magnetic diffusivity of the impellers compared to that of the fluid, gives an adequate interpretation of our experimental data.

4.2. Illustration: induction effects linked to helicity

When the fluid is set into motion by the rotation of a single impeller, the mean flow has a strong helical component. It results from the rotational entrainment and axial flow generated by the impeller acting as a centrifugal pump. When a transverse magnetic field is applied, this swirling motion induces an axial component through what has been termed the Parker effect [23]. Its

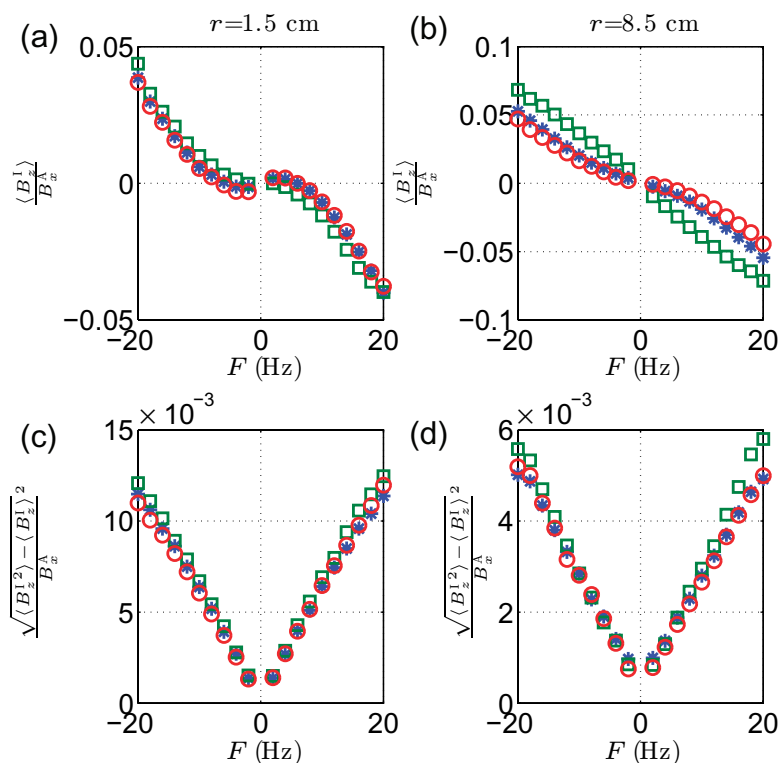


Figure 7. Evolution of the normalized time-averaged induced field $\langle B_z^I \rangle$ as a function of impeller rotation rate at radial position (a) $r/R = 0.15$ and (b) $r/R = 0.87$. Corresponding rms amplitudes in (c) and (d). Symbols: (\star) stainless steel impellers, (\circ) iron impellers and (\square) soft-iron impellers.

evolution with the impeller rotation rate is quadratic because it involves both the azimuthal and the axial velocity of the fluid. When impellers of high magnetic permeability are used, we expect an additional effect as described above, again being made accessible to measurements in the mid-plane because of the boundary condition at the vessel boundary. Moreover, this last effect is dominant at the lateral wall of the vessel, so we expect to observe (i) induction characteristics corresponding to the Parker effect near the axis of the cylinder (it varies quadratically with the impeller rotation rate) and (ii) induction characteristics associated with the solid rotation of the impeller in a transverse applied field near the wall, as described in the previous section (it varies linearly with the impeller rotation rate).

Our measurements correspond to $F_2 \neq 0$ and $F_1 = 0$ in the configuration sketched in figure 1(b). The applied field is transverse, $\mathbf{B}^A = -B_x^A \hat{x}$. The evolution of the time-averaged induced field $\langle B_z^I \rangle$ measured in the mid-plane is shown in figures 7(a) and (b) for the innermost probe in the array ($r/R = 0.15$) and the outermost probe ($r/R = 0.87$). As can be seen, in the center of the flow, the induction varies quadratically with the impeller rotation rate, in a manner that is independent of its material. On the other hand, nearer the outer wall, the evolution, initially quadratic, becomes linear when soft-iron impellers are used. In all cases, the fluctuations shown in figures 7(c) and (d) show no dependence on impeller material. These features are consistent with the interpretation given in the previous section.

5. Discussion and conclusions

Our observations show that driving von Kármán flows with ferromagnetic impellers has a significant impact on magnetic induction processes. The response of the flow to an externally applied magnetic field reveals additional contributions to the induced field. Moreover, at the intermediate magnetic Reynolds numbers probed with our gallium flow, the additional contributions vary linearly with the change in $\mu\sigma$ between fluid and impeller. Finally, as this additional contribution is associated with the (controlled) motion of the impellers, it has much less fluctuations than the induction originating solely from the flow velocity gradients.

Such effects may have a significant impact on dynamo processes in laboratory experiments. They could be quite important in the generation of the VKS dynamo [7]. Expanding on our observations, one may expect that the combination of velocity shear and magnetic diffusivity discontinuity at the impellers generates a quite strong ω -effect in the vicinity of soft-iron impellers. As a result, an axial magnetic field would be efficiently converted into a toroidal field in this region. For the regeneration of the axial field, several types of α -effects have been proposed [8]. In the above scenario, the VKS dynamo generates an axial dipole from α - ω processes that are both localized in the vicinity of the ferromagnetic impellers, which also have the following major contributions:

- Their large $\mu\sigma$ value and associated enhancement of induction effects (as measured in section 3.2) help bring a dynamo threshold within the range of R_m values accessible to the experiment.
- They promote an axial magnetic field. It would help understand why the actual dynamo field generated with soft-iron impellers is dominated by an axial dipole, in contrast with numerical simulations made for homogeneous magnetic conditions, which predicted a transverse dipole.
- The localization of dynamo sources near the impellers may help understand why the evolution of the VKS dynamo field shares many features with low-dimensional chaos [24], as would result from nonlinear interactions of two weakly coupled dynamos.

Further measurements will of course be needed. They involve the precise measurement of magnetic fields in the very vicinity of the impellers—an endeavor that requires major changes in the experimental setup and involves several technical challenges. Detailed induction measurements in the sodium (VKS) experiment would also be needed to clarify the evolution with the magnetic Reynolds, as the current gallium studies are restricted to R_m values of order unity.

Acknowledgments

The assistance of Marc Moulin is gratefully acknowledged. This work was funded under contract ANR-08-BLAN-0039-01.

References

- [1] Kageyama A, Sato T, Watanabe K, Horiuchi R, Hayashi T, Todo Y, Watanabe T H and Takamaru H 1995 Computer simulation of a magnetohydrodynamic dynamo 2 *Phys. Plasmas* **2** 1421–31
- [2] Müller U and Bühler L 2001 *Magnetofluidynamics in Channels and Containers* (Berlin: Springer)

- [3] Glatzmaier G A and Roberts P H 1995 A 3-dimensional convective dynamo solution with rotating and finitely conducting inner-core and mantle *Phys. Earth Planet. Interiors* **91** 63–75
- [4] Glatzmaier G A and Roberts P H 1996 An anelastic evolutionary geodynamo simulation driven by compositional and thermal convection *Physica D* **97** 81–94
- [5] Stefani F, Gailitis A and Gerbeth G 2008 Magnetohydrodynamic experiments on cosmic magnetic fields *Z. Angew. Math. Mech.* **88** 930–54
- [6] Verhille G, Plihon N, Bourgoin M, Odier P and Pinton J-F 2009 Laboratory dynamo experiments *Space Sci. Rev.* [0.1007/s11214-009-9546-1](https://doi.org/10.1007/s11214-009-9546-1)
- [7] Monchaux R *et al* 2007 Generation of a magnetic field by dynamo action in a turbulent flow of liquid sodium *Phys. Rev. Lett.* **98** 044502
- [8] Monchaux R *et al* 2009 The von Kármán sodium experiment: turbulent dynamical dynamos *Phys. Fluids* **21** 035108
- [9] Marie L, Burguete J, Daviaud F and Leorat J 2003 Numerical study of homogeneous dynamo based on experimental von Karman type flows *Eur. Phys. J. B* **33** 469–85
- [10] Oxley P, Goodell J and Molt R 2009 Magnetic properties of stainless steels at room and cryogenic temperatures *J. Magn. Magn. Mater.* **321** 2107–14
- [11] FEMM 4.2 2009 Finite elements method magnetics *Software* 4.2 <http://www.femm.info/>
- [12] Lide D (ed) 1994 *Handbook of Chemistry and Physics* 14th edn (Boca Raton, FL: CRC Press)
- [13] Daviaud F and Marié L 2004 Experimental measurement of the scale-by-scale momentum transport budget in a turbulent shear flow *Phys. Fluids* **16** 457–61
- [14] Odier P, Pinton J-F and Fauve S 1998 Advection of a magnetic field by a turbulent swirling flow *Phys. Rev. E* **58** 7397
- [15] Bourgoin M, Volk R, Frick P, Khripchenko S, Odier P and Pinton J-F 2004 Induction mechanisms in von Kármán swirling flows of liquid gallium *Magnetohydrodynamics* **40** 13
- [16] Bourgoin M, Odier P, Pinton J-F and Ricard Y 2004 An iterative study of time independent induction effects in magnetohydrodynamics *Phys. Fluids* **16** 2529
- [17] Ravelet F, Marié L, Chiffaudel A and Daviaud F 2004 Multistability and memory effect in a highly turbulent flow: experimental evidence for a global bifurcation *Phys. Rev. Lett.* **93** 164501
- [18] Volk R, Odier P and Pinton J-F 2006 Fluctuation of magnetic induction in von Karman swirling flows *Phys. Fluids* **18** 085105
- [19] Herzenberg A and Lowes F J 1957 Electromagnetic induction in rotating conductors *Phil. Trans. R. Soc. A* **249** 507–84
- [20] Weiss N O 1966 The expulsion of magnetic flux by eddies *Proc. R. Soc. A* **293**
- [21] Giesecke A, Stefani F and Gerbeth G 2009 Role of soft-iron impellers on the mode selection in the VKS dynamo experiment *Phys. Rev. Lett.* to appear (arXiv:0907.0123)
- [22] Nore C and Giesecke A 2009 Influence of ferromagnetic disks on the VKS dynamo private communication
- [23] Pétrélis F, Bourgoin M, Marié L, Burguete J, Chiffaudel A, Daviaud F, Fauve S, Odier P and Pinton J-F 2003 Nonlinear magnetic induction by helical motion in a liquid sodium turbulent flow *Phys. Rev. Lett.* **90** 174501
- [24] Ravelet F *et al* 2008 Chaotic dynamos generated by a turbulent flow of liquid sodium *Phys. Rev. Lett.* **101** 074502